Distinguishing Bulk Redox from Near-Surface Degradation in Lithium Nickel Oxide Cathodes

Lijin An[1], Jack E. N. Swallow[1], Peixi Cong[1], Ruomu Zhang[1], Andrey D. Poletayev[1,2], Erik Björklund[1,2], Pravin N. Didwal[1,2], Michael Fraser[1,2], Leanne A. H. Jones[1], Conor Phelan[1], Namrata Ramesh[1], Grant Harris,[5] Christoph J. Sahle[3], Pilar Ferrer[4], David C. Grinter[4], Peter Bencok[4], Shusaku Hayama[4], M. Saiful Islam[1,2], Robert House[1,2], Peter D. Nellist[1,2], Robert J. Green[5,6], Rebecca J. Nicholls[1], Robert S. Weatherup[1,2,4,]*

1 Department of Materials, University of Oxford, Parks Road, Oxford OX1 3PH, UK

2 The Faraday Institution, Quad One, Harwell Science and Innovation Campus, Didcot OX11 0RA, U.K.

3 ESRF – The European Synchrotron, 71 Avenue des Martyrs, 38000 Grenoble, France

4 Diamond Light Source, Harwell Science and Innovation Campus, Didcot OX11 0DE, U.K.

5 Department of Physics and Engineering Physics, University of Saskatchewan, Saskatoon, Canada S7N 5E2

6 Stewart Blusson Quantum Matter Institute, University of British Columbia, Vancouver, Canada V6T 1Z1

* robert.weatherup@materials.ox.ac.uk

ABSTRACT

Ni-rich layered cathodes deliver high energy densities, but uncertainties remain about their charge compensation mechanisms and the degradation processes that limit their cycle life. Recent studies have identified trapped molecular O_2 within $LiNiO_2$ at high states of charge, as seen for Li-rich cathodes where excess capacity is associated with reversible O^{2-}/O_2 redox. Here we show that bulk redox in $LiNiO_2$ occurs by Ni-O rehybridization, lowering the electron density on O sites, but without significant involvement of molecular O_2. Trapped O_2 is predominantly associated with surface degradation through contact with the electrolyte, and is accompanied by Ni reduction. O_2 is removed on discharge, but an excess of Ni^{2+} remains forming a reduced surface layer that impedes Li transport. Our findings highlight the importance of separating bulk redox from near-surface degradation, and implicate the instability of delithiated $LiNiO_2$ in contact with the electrolyte in surface degradation through O_2 formation.

KEYWORDS Molecular O_2, Lithium Nickel Oxide, Reduced Surface Layer, Anion Redox, Core Level Spectroscopy

INTRODUCTION

Layered transition metal oxides, $LiMeO_2$ (Me = Co, Ni, Mn, Al, etc.), are the cathode materials of choice for commercial high-energy density Li-ion batteries, reversibly intercalating Li over thousands of cycles.[1,2] Ni-rich materials are increasingly favoured as they offer higher capacities, and lower Co content, which is expensive and has ethical concerns around its extraction.[3] In the traditional picture of charge compensation, Li^+ removal is compensated by an increase in the formal oxidation state of the redox-active transition metal (TM) centres via single electron transfer. However, it is well-established that there are accompanying changes in Me-O bond covalency meaning both TM and O sites are involved.[4–7]

The archetypal Ni-rich cathode material, $LiNiO_2$, undergoes several first-order structural phase transitions on delithiation, and at high potentials degradation associated with severe lattice changes,[8,9] parasitic reactions[10–12], structural degradation[13,14] and gas evolution[15,16] become prominent. However the extent of the connections between these different modes of degradation is not yet fully established. There have recently been reports of trapped molecular O_2 formation in $LiNiO_2$ at high potentials (≥4.3V during charge), based on the emergence of a distinct feature in O K-edge resonant inelastic X-ray scattering (RIXS) spectra, corresponding to an excitation energy of ~531.5 eV.[17–19] For Li-rich materials that show excess capacity beyond TM cation redox, this is typically taken as evidence of the involvement of molecular O_2 in charge compensation.[20] Ni K-edge X-ray absorption Near Edge Structure (XANES) measurements of $LiNiO_2$ have indicated a plateauing of main edge half-height position at

similarly high states of charge, which has been taken as evidence of the formal Ni oxidation state no longer changing in the bulk,[19] and thus a change in the redox mechanism. [21]

Although O K-edge RIXS and the related fluorescence yield X-ray absorption spectroscopy (FY-XAS) are widely referred to as bulk-sensitive (~200 nm information depth), in the context of Li-ion cathode materials where typical secondary particle diameters are several μm or more, these methods probe <5% of the particle volume nearest to the surface. Attribution of bulk molecular oxygen redox based on these methods alone is therefore ambiguous, whilst reliable comparison to more bulk-sensitive XANES measurements is challenging, motivating the use of more bulk-sensitive probes of O redox.

Here we combine complementary core-loss spectroscopies to obtain a depth-resolved (10nm to >10 μm) account of the cation and anion redox processes in $LiNiO_2$, allowing reversible, bulk redox processes to be distinguished from near-surface degradation. X-ray Raman Spectroscopy (XRS, >10 μm information depth) reveals that in the bulk of $LiNiO_2$ secondary particles there is a continuous change in both the Ni $L_{3,2}$-edge and O K-edge spectra with SoC (state of charge) up to 4.8 V, consistent with charge compensation proceeding by rehybridization between the Ni and O centres, lowering the electron density on O sites but with coordination still preserved. Features of trapped molecular O_2 appear at potentials of ≳4.2 V in O K-edge FY-XAS, accompanied by increased Ni^{2+} contributions in the Ni $L_{3,2}$-edge. Importantly, these changes are less pronounced in bulk-averaged XRS measurements indicating a predominantly surface process. Total Electron Yield (TEY) measurements (~10 nm information depth) confirm a densified reduced surface layer (RSL) forms in direct contact

with electrolyte, whilst FY measurements are consistent with an extended cation mixing layer in which Ni^{2+} ions have migrated to occupy Li sites between the TM layers. Scanning Transmission Electron Microscopy - Electron Energy Loss Spectroscopy (STEM-EELS) further confirms this picture, showing that the RSL extends ~200 nm into the surface for $LiNiO_2$ which has been cycled to 4.8V vs. Li/Li^+. This understanding emphasises the importance of strategies to stabilise the interfaces of Ni-rich cathode materials in contact with electrolyte rather than bulk stabilisation approaches (e.g. pillaring) that might sacrifice capacity.

RESULTS AND DISCUSSION

Trends in Chemical State with SoC

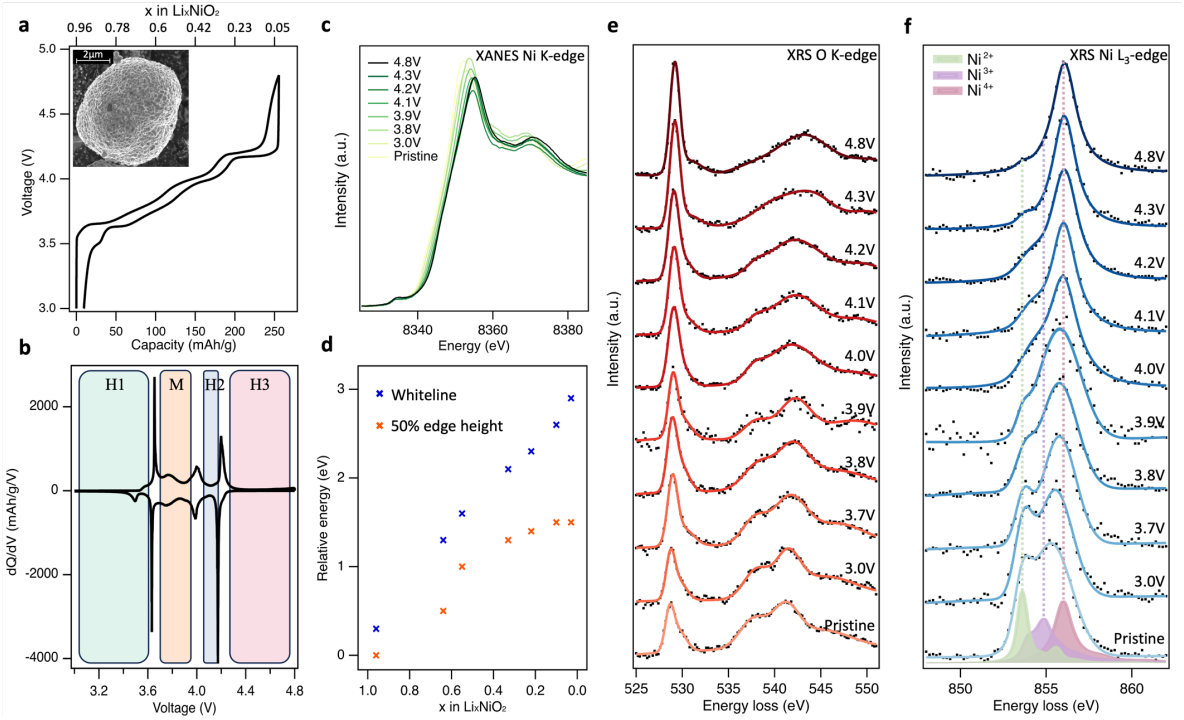

Fig. 1 | Bulk-sensitive Probing of $LiNiO_2$ Redox Processes. a, 2nd cycle charge-discharge profile of $LiNiO_2$ electrode cycled at a rate of C/20 between and 3.0 and 4.8 V vs Li/Li^+. Inset: SEM image of pristine $LiNiO_2$ particles. **b**, Corresponding differential capacity plots (dQ/dV). **c**, Normalised Ni K-edge XANES spectra (transmission mode) of $LiNiO_2$ at different SoC. **d,** Plot of the relative shifts in Ni K-edge whiteline and 50% normalised edge height positions. **e,f,** XRS (~10 μm information depth) of the O K-edge and Ni L_3-edge core-loss spectra for $LiNiO_2$ electrodes at different SoC during the 2nd charge cycle. Experimental XRS data is marked in black dots and represented in smooth solid trace lines. See Supplementary Fig. 9 for fitted XRS Ni $L_{3,2}$-edges using simulated formally Ni^{2+}, Ni^{3+}, and Ni^{4+} L_3-edge spectra from charge transfer multiplet (CTM) calculations.

The charge-discharge profile for the 2nd cycle of the composite polycrystalline $LiNiO_2$ electrode are shown in Fig. 1a. together with an inset showing a scanning electron micrograph (SEM) of the $LiNiO_2$ active material. In the image ~5 μm diameter spheroidal $LiNiO_2$ secondary particles are seen being composed of sub-μm primary particles. The voltage profiles show distinct plateaus associated with the first-order structural phase transitions of $LiNiO_2$ on delithiation, with their potentials apparent as maxima in the dQ/dV plots (Fig. 1b), at potentials consistent with prior literature.[22–26] Powder X-ray diffraction (XRD) of the pristine material (see Supplementary Fig. 1) closely resembles the calculated pattern for $LiNiO_2$ with the $R\bar{3}m$ space group.[27] This H1 (hexagonal) phase transitions to a M (monoclinic) phase at ~3.67 V, then to the H2 phase at ~4.0 V, followed by the H3 phase at ~4.2 V. The voltage profile shows noticeable hysteresis above ~4.3 V, with the voltage rapidly dropping from 4.8 V to ~4.2 V on discharge. However, the capacity reached at 4.8 V is 256 mAh/g which compares with a maximum theoretical capacity of 264 mAh/g for the $LiNiO_2$, based on the pristine material having ~4 % Ni excess as determined by inductively coupled plasma-optical emission spectroscopy (ICP-OES). This provides an initial indication that the full capacity of the electrode can be accounted for by Ni redox alone, without obvious excess capacity associated with molecular O_2 redox.

Fig. 1c shows normalised transmission Ni K-edge XANES spectra for the $LiNiO_2$ electrodes at different states of charge during the 2nd charge cycle. As expected, the Ni K-edge shifts to higher energies as the Ni oxidation state increases, as the removal of valence electrons leaves

the Ni nucleus less-shielded such that the nucleus has a higher effective charge, and the core-level becomes more strongly bound. Both the energy of the fractional (normalised) edge height and the position of the whiteline (intensity maximum) are routinely used as indirect measures of average oxidation state.[28–30] A continuous shift to higher energy in both the edge half-height and whiteline is observed up to 4.2 V, x=0.22 (Fig. 1d). The two trends diverge with further delithiation, with the whiteline monotonically shifting to higher energy up to the furthest measured extent of delithiation (4.8V, x=0.03), while the half-height position plateaus with little variation between x=0.10 and x=0.03. The plateau of half-height position has previously been taken as an indication that Ni is no longer involved in the redox mechanism at high SoC,[21,31] however the continuing shift in whiteline position would suggests otherwise. Indeed, the edge-position is known to be sensitive to other factors including bond length and ligand covalency.

To resolve this ambiguity without introducing surface sensitivity as a confounding factor, bulk-sensitive X-ray Raman Scattering (XRS) was performed to collect O K-edge (Fig. 1e) and Ni L_3-edge (Fig. 1f) spectra at the same SoC as the XANES. XRS allows low energy O 1s→2p and Ni 2p→3d transitions to be measured using a hard X-ray probe (10 keV), achieving an information depth of ~10 μm which is similar to Ni K-edge XANES. In Fig. 1e, pristine $LiNiO_2$ exhibits a prominent asymmetric O K pre-edge feature centred at 528.8 eV associated with transitions from O 1s→O 2p-Ni 3d hybridised states, and main edge features above 535.0 eV associated with transitions from O 1s→O 2p-Ni 4s,p hybridised states. On delithiation, the pre-edge peak is seen to continuously increase in relative intensity, whilst losing its asymmetry

and shifting by 0.4 eV to a higher peak energy of 529.2 eV. There is also an accompanying shift in the main edge half-height from ~536.0 eV for pristine $LiNiO_2$ up to 539.5 eV at 4.8 V. Importantly, across the potentials probed, the feature arising at ~531.5 eV associated with the formation of molecular O_2 is not strongly pronounced.[17–19]

The corresponding Ni L_3-edge XRS (Fig. 1f) for pristine $LiNiO_2$ shows a broad, nearly trapezoidal line shape composed of three main features at 853.6 eV, 854.9 eV, and 856.1 eV. Although there remains debate over the ground state of $LiNiO_2$ (see supplementary note 1), recent temperature-dependent XAS and X-ray Magnetic Circular Dichroism (XMCD) shows strong evidence for size (spin) disproportionation,[32] in which Ni^{2+} (S=1), Ni^{3+} (S=½), and Ni^{4+} (S=0) octahedra coexist and interconvert dynamically at room temperature. These three species are attributable to the 853.6 eV, 854.9 eV, and 856.1 eV features respectively.[33] This contrasts with the singular formal $3d^7$ ground-state electron configuration expected for Ni^{3+} within a pure Jahn-Teller formalism, but is consistent with other correlated nickelate compounds, including $AgNiO_2$, which show disproportionation and strong covalency between frontier O 2p and Ni 3d states.[34–37] Charge transfer multiplet (CTM) calculated $L_{3,2}$-edges for the three Ni environments are overlaid in Fig. 1f. These simulated spectra can be thought of as a superposition of metal-ligand hole configurations,[38] with the formally Ni^{2+}, Ni^{3+}, and Ni^{4+} octahedra having ground-state configurations of $0.80|3d^8\rangle + 0.19|3d^9\underline{L}\rangle + 0.01|3d^{10}\underline{L}^2\rangle$, $0.25|3d^7\rangle + 0.58|3d^8\underline{L}\rangle + 0.16|3d^9\underline{L}^2\rangle + 0.01|3d^{10}\underline{L}^3\rangle$, $0.04|3d^6\rangle + 0.33|3d^7\underline{L}\rangle + 0.48|3d^8\underline{L}^2\rangle + 0.14|3d^9\underline{L}^3\rangle + 0.01|3d^{10}\underline{L}^4\rangle$ respectively. The increasing ligand

hole contributions indicate an increasing degree of Ni-O covalency for higher formal oxidation states. Linear combinations of the simulated spectra match closely to Ni L_3-edge XRS spectra (Supplementary Fig. 9).

On cycling to higher potentials, the Ni^{4+} feature is seen to continuously grow in intensity (see Fig. 2d), initially at the expense of the Ni^{2+} up to 3.9V (x=0.55), and then the Ni^{3+} up to 4.8V (x=0.03). This evolution of Ni species upon delithiation matches that expected from the disproportionation of NiO_6 octahedral sizes.[32] At 4.8V, the spectrum closely matches Ni L_3-edge simulations of Ni^{4+} (Supplementary Fig. 4) with up to 4-5% concentration of antisite Ni_{Li} and its charge compensation. The bulk sensitivity of XRS suppresses contributions from reduced surface layers which are otherwise seen even for inverse partial fluorescence yield (IPFY) measurements (Supplementary Fig. 2), including for reference Ni^{4+} compounds.[39,40] Importantly this shows that charge compensation in the $LiNiO_2$ bulk proceeds predominantly through Ni-O rehybridization across the whole cycling range, lowering the electron density on O sites but without a significant role of molecular O_2 redox. This contrasts with several reports of oxygen redox in this potential range for $LiNiO_2$ and Ni-rich layered cathode materials, based on detection of the molecular O_2 feature with less bulk-sensitive O K-edge RIXS.[17,19,41,42]

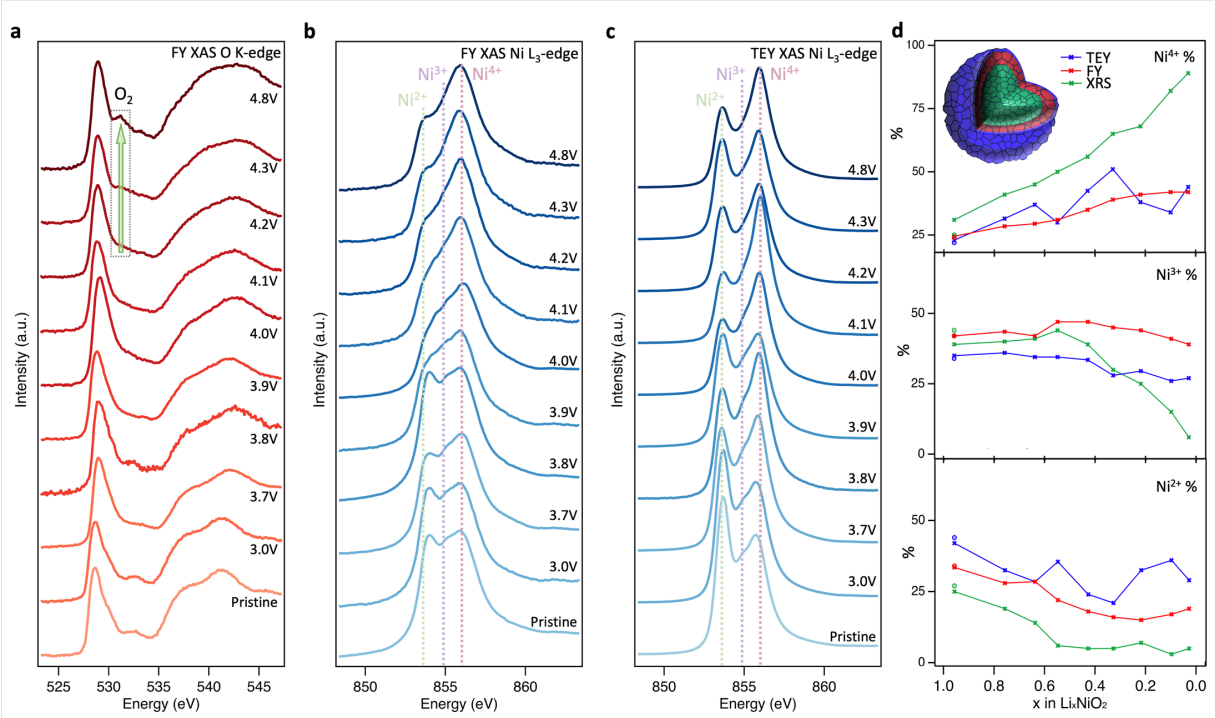

Fig. 2 | Near-surface probing of $LiNiO_2$ redox processes. a,b, FY-XAS (~200 nm information depth) of the O K-edge and Ni L_3-edge, and **c,** TEY-XAS (~10 nm information depth) of the Ni L_3-edge for $LiNiO_2$ at different SoC. **d**, Relative intensities of Ni^{2+}, Ni^{3+}, and Ni^{4+} components based on fitting CTM calculated spectra to XRS, FY-XAS, and TEY-XAS spectra (see fitting results in Supplementary Fig. S9-11).

To further investigate the origins of molecular O_2 reported at high SoC, the same core levels were measured using soft XAS in FY mode (Fig. 2a,b). The spectra for pristine $LiNiO_2$ closely resemble those obtained with XRS, however an additional feature is apparent at 532.3 eV in the O K-edge, and the Ni^{2+} feature in the Ni L_3-edge is more intense at 4.8 V. These same features are seen for NiO (see Supplementary Fig. 14),[43] and correspond to a thin (<5 nm) NiO-

like reduced surface layer (RSL),[44,45] whose contribution is not detected in the more bulk-sensitive XRS. On delithiation, the XAS data show similar trends to the XRS until 4.1 V (x=0.33), with the Ni L_3-edge showing the Ni^{4+} feature increasing at the expense of Ni^{2+}, and some growth in the O K pre-edge. At higher SoC there are significant deviations between FY and XRS spectra. Most notably a feature at ~531.5 eV is seen to emerge in the O K-edge, which although initially weak at 4.2V shows significant intensity at 4.8V (see integrated peak areas in Supplementary Fig. 3). This feature corresponds to the same absorption energy as molecular O_2, whose vibrational structure has been detected in $LiNiO_2$ and other conventional Ni-rich layered oxides in several recent reports.[18,19,42] Alongside the emergence of this feature, the growth in the O K pre-edge peak and the Ni^{4+} feature in the Ni L_3-edge are supressed in FY compared to the XRS, whereas the Ni^{2+} feature grows. This suggests a near-surface molecular oxygen redox process associated with RSL growth, i.e., $NiO_2 \rightarrow NiO_{2-x} + \frac{1}{2}xO_2$. Similar trends are observed with the more surface-sensitive TEY-XAS (fits in Supplementary Fig. 11) consistent with RSL formation proceeding from electrolyte-exposed surfaces.[44,46]

Fig. 3a shows that after cycling back down from an upper cutoff voltage (UCV) of 4.8 V to 4.0 V, already the molecular O_2 feature at ~531.5 eV disappears from the O K-edge, but a prominent RSL feature at 532.6 eV emerges. On cycling down to 3.0 V, the RSL feature further grows in intensity relative to the pre-edge feature, and accompanying increases in the Ni^{2+} feature are observed in the Ni L_3-edge spectra (Fig. 3b,c). This is even more prominent in the surface-sensitive TEY-XAS (Fig. 3c), indicating densification of the RSL near to the surface. Comparison to an electrode where the UCV is 4.2 V confirms that the extent of RSL formation

is much greater for the UCV of 4.8V, consistent with previous studies where significant RSL formation occurs at SoC above the H2-H3 transition in Ni-rich cathodes.[44,46–48] This highlights a key connection between the formation of trapped molecular O_2 and the increase in Ni^{2+} species near the cathode surface.

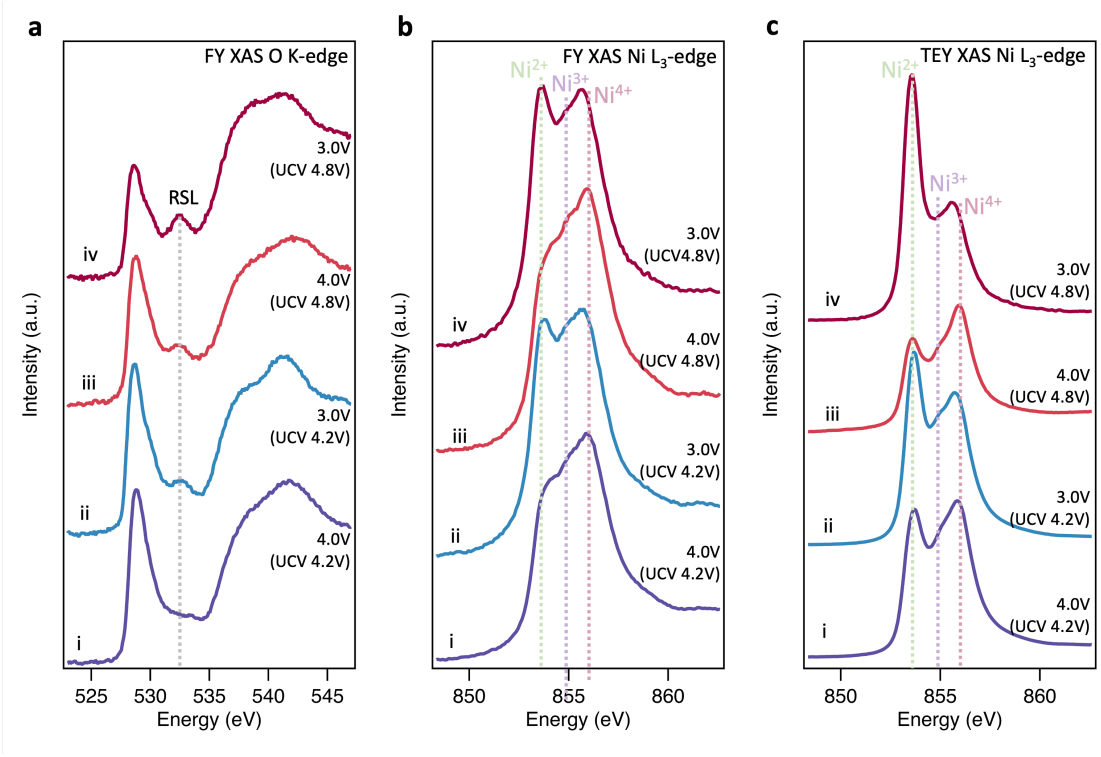

Fig. 3 | Discharge behaviour of $LiNiO_2$. a,b, FY-XAS (~200 nm information depth) of the O K-edge and Ni L_3-edge, and **c,** TEY-XAS (~10 nm information depth) of the Ni L_3-edge for $LiNiO_2$ cycled to a UCV of 4.2 V before being discharged to (i) 4.0 V and (ii) 3.0V, with parallel samples continued cycling to a higher UCV of 4.8 V and then back to (iii) 4.0 V and (iv) 3.0V respectively.

Depth Dependence of Chemical Species with EELS

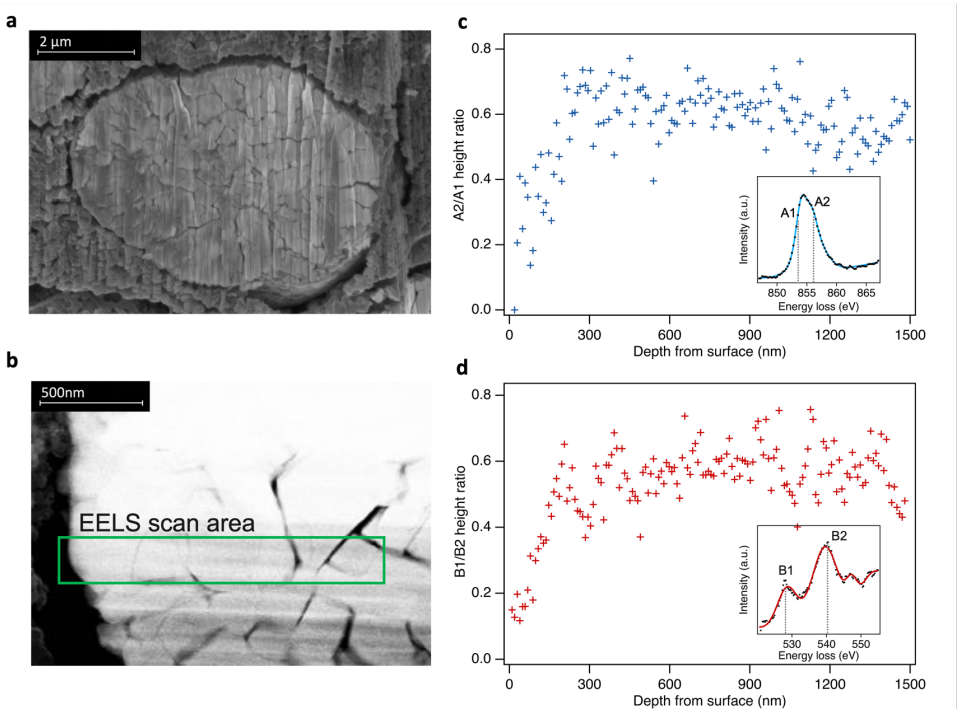

Fig. 4 | a, Cross-sectional scanning electron microscopy (secondary electron detection) of $LiNiO_2$ particle from an electrode charged to 4.8 V. **b**, Selected STEM-EELS scan area of 1.5 µm from surface to bulk (left to right) of the particle. **c,d,** Fitted peak ratios of depth-resolved Ni L_3- and O K-edge EELS spectra using a simplified two peak fit in each case . Insets: examples of fitted EELS spectra.

Although comparison of TEY and FY mode XAS confirms the RSL is found predominantly near the sample surface, it provides only limited insight into the depth over which it is distributed. In order to spatially resolve the extent of the RSL at high SoCs, scanning transmission electron microscopy - electron energy loss spectroscopy (STEM-EELS) was performed for 4.8 V $LiNiO_2$ (x=0.03) sample (Fig. 4). Depth-resolved Ni L_3- spectra of charged

4.8 V $LiNiO_2$ show an increasing proportion of the higher energy (more oxidised) component on moving towards the bulk of the particle, stabilising at ~200nm from surface, consistent with more Ni^{2+} species at the surface and more Ni^{4+} in the bulk. Similarly the O K-edge EELS shows a higher pre-edge intensity towards the bulk of the particle correlating with higher Ni oxidation state and Ni-O covalency.[49] This extended RSL region where the Ni oxidation state is seen to vary over ~200 nm, is consistent with the differences seen between TEY-XAS, FY-XAS and XRS observations. Notably, a similar extent of RSL formation is not observed at intergranular cracks away from the $LiNiO_2$ surface, presumably as electrolyte does not fully penetrate these cracks for the low cycle numbers considered here. This indicates a key role of the electrolyte in promoting RSL formation, with electrolyte infiltration into internal cracks likely proceeding over multiple cycles.

Bulk Electronic Structure Evolution of $LiNiO_2$ on delithiation

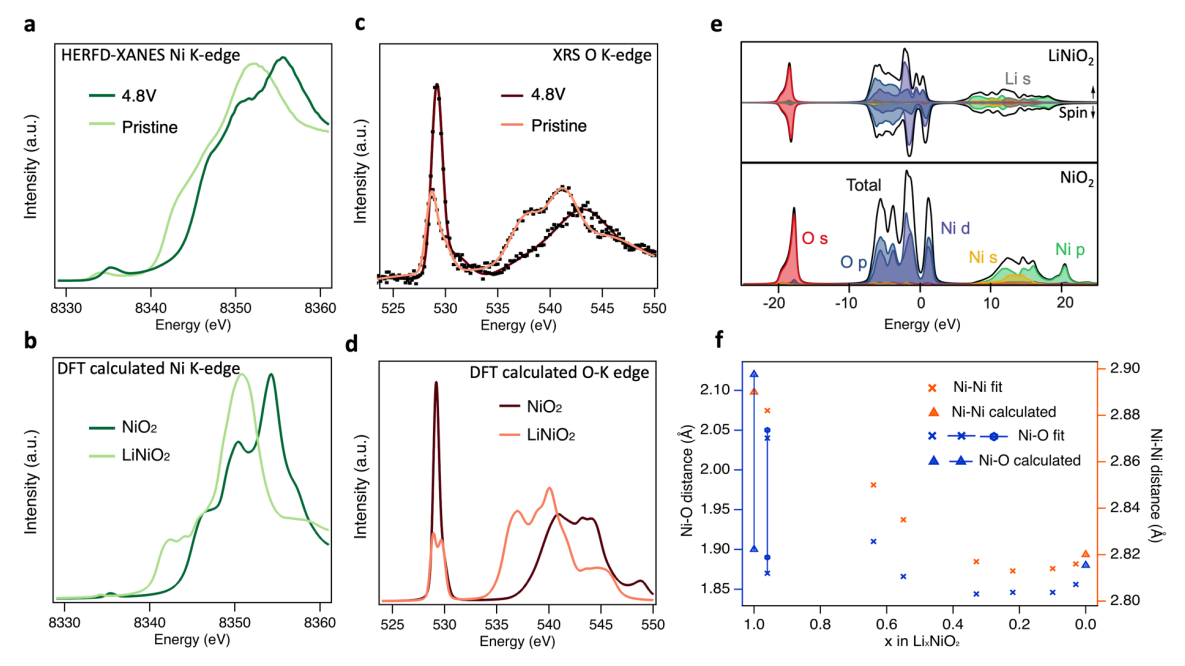

Fig. 5 | Electronic and Structural Changes of $LiNiO_2$ upon delithiation. a, Experimental HERFD-XANES and **b**, core-hole calculated Ni K-edge spectra of pristine and charged $LiNiO_2$. **c**, Experimental XRS with smooth trace lines and **d**, core-hole calculated O K-edge spectra of pristine and charged $LiNiO_2$. **e**, Ground-state partial and total density of states for $LiNiO_2$ (top) and NiO_2 (bottom). Fermi energies are set to zero. **f**, Ni-Ni and Ni-O bond distances determined from the Fourier-transformed EXAFS spectra of Fig. 1c. Note that the short/long Ni-O lengths of pristine (hexagons) and 3.0 V (crosses) $LiNiO_2$ are related to the size-disproportionated model applied for EXAFS fitting. Bond lengths for the $P2_1/c$ structure used for DFT calculations in (b,d,e) are shown as "calculated" in (f).

Having shown that bulk redox in $LiNiO_2$ occurs by Ni-O rehybridization, we now consider further the associated changes in geometric and electronic structure. Fig. 5a shows high-energy-resolution fluorescence detection (HERFD-)XANES Ni K-edge spectra of pristine $LiNiO_2$ and after cycling to 4.8V. Notably the main edge half-height position is shifted ~2.1 eV higher in energy compared to $LiNiO_2$, a more distinct change than that seen in the transmission mode measurements of Fig. 1c (~1.5 eV), as a result of the fine-structure features along the rising edge now being better resolved. Fig. 5c compares the similarly bulk-sensitive experimental O K-edge XRS spectra of the same samples. Since we can anticipate that differing Ni-O bond lengths are likely to yield different signatures in the O K pre-edge, in any model of the material, we chose the zigzag $P2_1/c$ structure for $LiNiO_2$ spectral calculations. Density functional theory (DFT) calculated Ni and O K-edge spectra for $LiNiO_2$ and NiO_2 (Fig. 5b,d), reproduce the features of the experimental spectra extremely well, showing the same pre-edge peaks, number of fine structure features, and similar trends in intensity and linewidths across the whole spectral range. The relative energy shifts are also captured well, giving confidence in the sufficiency of the chosen structure models ($P2_1/c$ for $LiNiO_2$, and $R\bar{3}m$ for NiO_2).

The origin of the spectral features can be understood by comparison to ground-state partial density-of-states (pDOS) shown in Fig. 5e, and consideration of the allowed spectroscopic transitions. The first unoccupied states in both $LiNiO_2$ and NiO_2 lie just above 0 eV, showing mixed O 2p and Ni 3d orbital character and giving rise to the pre-edge peaks in the Ni (~8335 eV) and O (~529 eV) K-edges. A sizable gap separates the next set of unoccupied states which

give rise to the main edges in the Ni (≳8340 eV) and O (≳55 eV) K-edges, and have Ni 4s,p character, with some Li 2s contribution also seen in this region for $LiNiO_2$. This gap widens by ~2.9 eV from $LiNiO_2$ to NiO_2 which can be related to decrease in average Ni-O bond length associated with the change in geometric structure.[50,51] We note that the DFT calculated Ni K-edge spectra show weaker pre-edge features than experiment, attributable to quadrupolar transitions not being considered in the calculations.[52]

The XRS O K pre-edge becomes far more intense in the 4.8V sample and the peak splitting in calculated spectrum of NiO_2 is lost, forming a single symmetric peak. This is consistent with the increased ligand hole contributions for the Ni^{4+} octahedra from the CTM calculations, which indicates an increasing degree of Ni-O covalency on delithiation. A clear splitting of the O K pre-edge peak in the calculation for $P2_1/c$ $LiNiO_2$ resembles the asymmetric pre-edge in the experimental data. This corresponds with the change from D_{4h} symmetry for the J-T distorted Ni^{3+} octahedra used in the calculation, where d orbital splitting arises from the elongation of two Ni-O bonds, to O_h symmetry for the Ni^{4+} octahedra of NiO_2, where this d orbital splitting is lost. The growth in intensity of the O K pre-edge feature by a factor of ~2 on full delithiation (see Supplementary Fig. 3) is consistent with an increase in covalency and therefore ligand holes, corresponding closely with a factor of ~1.8 obtained based on the proportions of Ni species fitted to the Ni $L_{3,2}$-edge XRS spectra (Fig. 2d) and their respective electron configurations. Further evidence for increased Ni-O covalency on delithiation is apparent from the emergence of more distinct fine-structure features (~8347 eV and 8351 eV) in the Ni K-edge, attributable to LMCT shakedown transitions,[53,54] as well as satellite peaks in the Ni $L_{3,2}$-edge that are most clearly

seen FY measurements (see Supplementary Fig. 8b) and well-reproduced in the CTM calculated Ni^{4+} spectrum. Moreover, Bader charge analysis based on the ground-state DFT calculations shows the ionic charge of the Ni only modestly changes from +1.41 to +1.56 e^- between the $P2_1/c$ $LiNiO_2$ and $R\bar{3}m$ NiO_2 structures, whilst a more significant change from -1.15 to -0.78 e^- is seen for the O charges.

Fig. 5f shows the nearest Ni-O and Ni-Ni distance extracted by fitting to EXAFS spectra for the $LiNiO_2$ at different SoC. Since single Ni-O bond length model fit showed significantly higher Debye-Waller factors for close to fully lithiated samples, a size-disproportionated model (58:42 ratio of short:long Ni-O bonds) was instead used for pristine and 3.0 V $LiNiO_2$ (see Supplementary Fig. 7, Supplementary Table 2). The Ni-O and Ni-Ni bond lengths thus obtained show good agreement with the extracted structural parameters of geometry optimised structures from our DFT calculation ($P2_1/c$ $LiNiO_2$).

Similar trends in weighted average Ni-O bond lengths are seen to *operando* neutron diffraction measurements,[55] with Ni-O bond length gradually shrinking in line with the change in structure and increased oxidation state and covalency at high SoC. Notably, above the H2-H3 transition ($x \leq 0.22$) a modest increase in the Ni-O bond length is observed. This has been associated with a loss of the stabilising effect of Li-O covalency at high SoC, leading to Ni-O bond elongation alongside the sudden c-lattice collapse related to the H2-H3 transition, and increased charge transfer from the O to Ni sites.[56–59] This changing covalency, seen as continuous spectral changes in Fig. 1c,d, can account for the plateauing in half-height position of the Ni K main-edge at high SoC in transmission XANES (Fig. 1d). As well as highlighting

the limitations of applying a single metric to assess changes in oxidation state, the limited sensitivity of the Ni K-edge fractional-edge height, reflects that it arises from transitions to Ni 4s,p states, in contrast to the O K- and Ni $L_{3,2}$-edges which probe transitions to O 2p-Ni 3d hybridised states.

Bulk Charge Compensation Mechanism and Surface Degradation

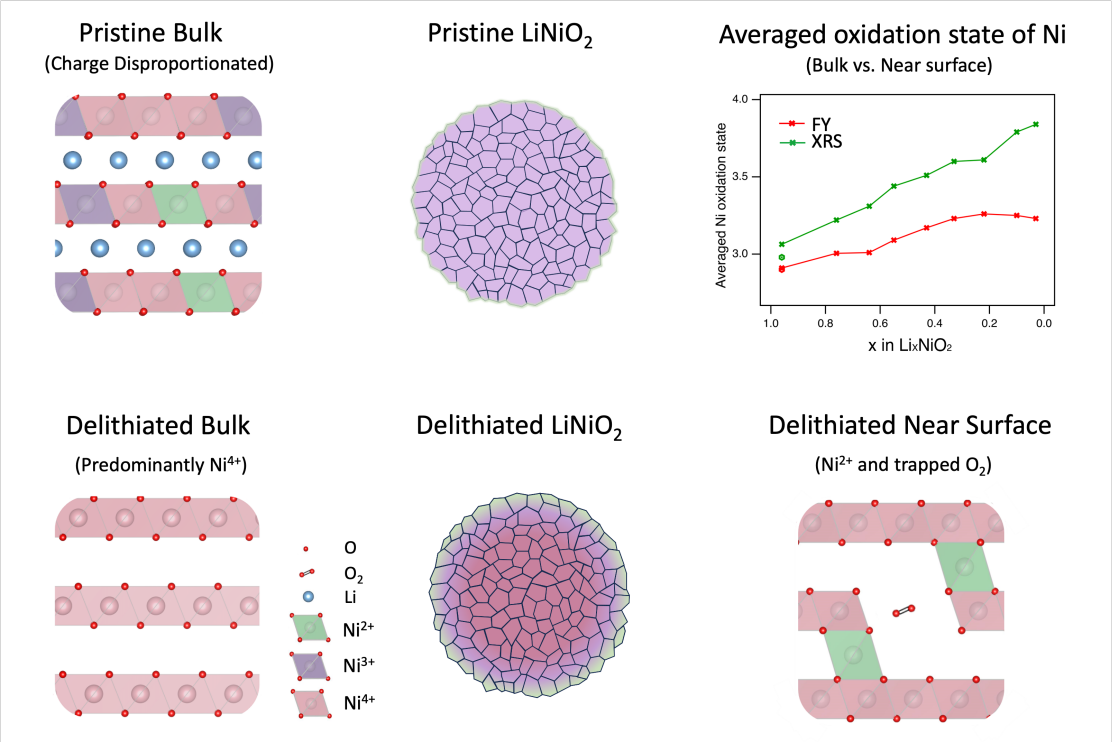

Fig. 6 | Schematic representation of pristine and delithiated $LiNiO_2$ particles. The differences on $LiNiO_2$ delithiation occurring at the surface and in the bulk, including the accommodation of trapped O_2 in pores formed near the surface by Ni^{2+} species migrating to the Li layer. Continuous oxidation of Ni in bulk $LiNiO_2$ at high SoC is distinguished from the near surface degradation. The averaged bulk and near surface Ni oxidation state of pristine $LiNiO_2$ are marked with hexagons.

In summary, bulk sensitive XRS measurements reveal that in the bulk of $LiNiO_2$, charge compensation occurs by Ni-O rehybridization. From an initially size disproportionated structure where Ni^{2+}, Ni^{3}, and Ni^{4+} octahedra coexist, the Ni^{4+} feature of the Ni $L_{3,2}$-edge is seen

to continuously grow, initially at the expense of Ni^{2+} and subsequently Ni^{3+} features (see Figure 6). There is a concomitant increase in O K pre-edge intensity, consistent with significant lowering of electron-density on the O sites at high SoC, where O loss is expected.[40,60] However, significant signatures of molecular O_2 formation are not detected throughout the bulk suggesting its formation remains kinetically hindered.[61]

FY measurements reveal evidence of molecular O_2 formation in the outer ~200 nm of the cathode surface, with the growth in intensity of the Ni^{4+} feature plateauing above 4.2 V, and features of trapped molecular O_2 emerging alongside increased Ni^{2+} contributions. This is consistent with molecular O_2 becoming produced in voids formed by Ni^{2+} entering the Li layers (see Fig. 6). STEM-EELS reveals a RSL that extends over ~200 nm into the $LiNiO_2$ surface following cycling to 4.8 V, and shows a gradual change in oxidation state across its thickness consistent with the formation of a cation disordered phase. The absence of such an extended RSL at internal surfaces of the secondary cathode particles, e.g. interparticle cracks, suggests formation of the extended cation disordered phase is driven by contact with the electrolyte.

The trapped molecular O_2 feature disappears on discharging to 4.0 V, but a significantly increased near-surface Ni^{2+} contribution is retained. Although our results do not fully exclude some reversible molecular O_2 redox, online electrochemical mass spectroscopy (OEMS) studies have also reported O_2 evolution occurring on discharge,[62] which we suggest may arise from trapped O_2 release associated with the structural changes occurring on discharging as a result of abrupt c lattice expansion, including particle cracking (Supplementary Fig. 5).

Our findings highlight the need for bulk-sensitive studies to fully confirm the extent to which molecular O_2-redox processes in cathode materials are bulk phenomena that contribute to excess capacity, rather than surface-mediated degradation. The understanding developed of the surface instability of NiO_2 associated with rehybridisation at high SoC, emphasises the importance of strategies such as cathode coatings, and changes in electrolyte formulation in order to stabilise Ni-rich cathode surfaces in contact with electrolyte, rather than bulk stabilisation approaches (e.g. pillaring) that might unduly sacrifice capacity.

METHODS

Sample Preparation

Commercial grade $LiNiO_2$ powder was obtained from BASF, without any deliberate doping or coating added. Free-standing electrodes were prepared by calendaring the mixture of 80 wt% $LiNiO_2$ powder, 10 wt% conductive acetylene black and 10 wt% polytetrafluoroethylene (PTFE) binder. Electrochemical tests of the $LiNiO_2$ cathodes were performed in 2032 coin cells (316 stainless steel, Cambridge Energy Solutions) using Li metal disks as negative electrodes and borosilicate glass fibre separators (borosilicate, GF/A, Whatman) soaked with 120 μL LP57 electrolyte (1M LiPF6 in 3:7 of EC:EMC). The assembled cells were charged up to 4.2 V and back to 3.0 V at C/20 (calculated based on a theoretical capacity of $LiNiO_2$ of 275mAh/g), followed by a second charge up to different voltages at C/20. All potentials mentioned in this work are referenced to Li/Li^+.

Electron Microscopy

A Thermo Scientific Helios G4 CXe Plasma FIB (PFIB) was used to prepare the STEM lamellae. For lift-out, a thin Pt layer was deposited onto the surface region of interest (ROI), trenches were patterned around the ROI to make 4 μm-thick lamellae. A W needle was then used to lift each lamella and place them on a FIB lift-out grid (Cu, Agar Scientific). Each lamellae was then thinned down to around 50nm thick for STEM-EELS and polished with a low dose, low energy beam (<0.3 nA, 5kV) to minimise ion beam damage. Inert transfer between PFIB and an Ar glovebox was achieved using a Gatan iLoad system.

Spatially resolved electron energy loss spectroscopy (EELS) of the lamellae was performed using a JEOL ARM200F equipped with cold field emission gun operated at 200 kV and spherical aberration probe corrector. Dual EELS was acquired using a Gatan GIF Quantum 965 ER with energy resolution of around 1eV at 0.25eV/channel dispersion. Inert transfer between glovebox and STEM was achieved using a JEOL double-tilt vacuum transfer holder.

Given $LiNiO_2$ is less stable when highly delithiated, radiation damage should be considered when evaluating the oxidation state of Ni in EELS. The energised Xe ion beam in PFIB and electron beam in STEM can both induce reduction of $LiNiO_2$ and NiO_2 towards NiO.[63] Low doses of for STEM-EELS study of 3×10^3 $e^-/Å^2$ were used, the absolute A2/A1, and B2/B1 ratios seen in the $LiNiO_2$ bulk reflect some degree of ion/electron beam induced reduction. Nevertheless, equal acquisition time and constant electron beam current during the EELS scans ensure a consistent radiation dose such that the trends in EELS spectra and the spatial variations seen near their surface are still valid.

X-ray Spectroscopy

Transmission Ni K-edge XANES and EXAFS spectra were collected with a laboratory-based easyXAFS300+ spectrometer (easyXAFS, WA, US). X-rays are generated with a liquid-cooled Ag anode X-ray tube, before monochromation by a Si (551) spherically bent crystal analyser. A helium-filled box with polyimide windows is placed in the beam path for better X-ray transparency while a steel plate with a 9×3 mm slot is placed after each sample to lower the background. The transmitted intensity is measured with an SDD detector (KETEK, Munich, Germany) placed behind the sample. Each acquisition was performed over 45 min and 30 scans

were collected for each sample to obtain good statistics. NiO reference spectra were also collected for each batch of measurements for energy calibration. Data pre-processing was performed with the EasyXANES package to convert the measured intensity into linear attenuation coefficient, μ. EXAFS data reduction and analysis were performed using the Demeter package (version: 0.9.26).

HERFD-XANES measurements were collected at the I20 (scanning branch) beamline at Diamond Light Source. A four-bounce Si (111) monochromator is employed for incident X-ray energy selection. The [444] reflection off the three Si (111) spherically bent crystal analysers (bending radius of 1 m) from the multi-crystal spectrometer was used for the selection of Ni $K\beta_{1,3}$ emission line (approximately 8266 eV).

TEY and FY XAS measurements were performed at ES-2 of beamline B07-B at Diamond Light Source, with the exit slits set to 50 μm in the dispersive direction, yielding a flux of between 1×10^{11} (O K-edge) and 2×10^{11} (Ni $L_{3,2}$-edge) photons/s. All samples were measured with the incident beam normal to the electrode surface, yielding a beam footprint of 150 × 100 μm. FY measurements were acquired using an Al coated Si photodiode directed at the sample with its surface normal at ~45° to incident beam direction. Simultaneous TEY measurements were obtained using a SR570 low-noise current amplifier (Stanford Research Systems) to collect the current between the sample plate and an isolated steel washer in front of the sample biased to +90 V. Separate IPFY XAS measurements of the Ni $L_{3,2}$-edge were acquired using a Vortex silicon drift detector (Hitachi) at the I10 beamline, Diamond Light Source (Harwell),

with FY and TEY measurements simultaneously acquired. All spectra are divided by the drain current measured from the last X-ray mirror, to correct for variations in incident photon flux. The photon energy scale is calibrated using a NiO sample.[64] O K-edge spectra are background-subtracted using a straight line fitted to the pre-edge region, followed by intensity normalization to the post-edge region at 550 eV. Ni $L_{3,2}$-edge spectra are normalized to the intensity at 867eV after removal of a linear background.

XRS measurements were performed at the European Synchrotron Radiation Facility at the ID20 beamline.[65] X-rays are generated from three U26 revolver undulators, before being collimated, and then monochromated by a liquid-nitrogen cooled double-crystal Si(111) pre-monochromator. The beam from a second Si(311) channel-cut post-monochromator is focussed onto a ~20×20 μm^2 spot at the sample position by a mirror in Kirkpatrick-Baez geometry. The sample surface was positioned at a grazing angle of ~1° relative to the incident beam direction, to maximise the illuminated area and the sample was scanned over a region of ~10 mm during the 4-hour measurement to minimise beam-induced changes. Inelastically scattered photons were recorded using 72 spherically bent Si(660) crystal analyser with energy loss events in the vicinity of both O K-edge and Ni $L_{3,2}$-edge. O K- and Ni $L_{3,2}$-edges were recorded at momentum transfers of q=6.9±0.5, and all data extraction and treatment were performed as described in ref 67. [66]

Charge-Transfer Multiplet Calculations

Ni $L_{3,2}$-edge multiplet simulations were performed at the ligand field level of theory using the many-body code, Quanty.[67] This was implemented using the same single-cluster NiO_6 Hamiltonian as Green et al.,[68] where Ni 2p, Ni 3d ligand shells are explicitly included (see full detail in Supplementary Note 3). For all calculations, Slater integrals are scaled to 80% and 85% for the initial and final Hamiltonians respectively. Additionally, onsite ligand energy shifts of T_{pp}=±0.75 eV were applied to the ligand orbitals of e_g (+) and t_{2g} (-) symmetry.

Parameters used in Ni^{2+} calculation (eV): Δ= 5.5, $10D_q$= 0.71, V_{eg}= 2.627, V_{t2g}= 1.524.

Parameters used in Ni^{3+} calculation (eV): Δ = -0.5, $10D_q$= 0.93 with Jahn-Teller splitting of Δ_{eg}= 0.15 and Δ_{t2g}= 0.10 where Δ_{eg} is the difference between the $x^2 - y^2$ and $3x^2 - r^2$ onsite energies and Δ_{t2g} is the difference between the xy and xz/yz onsite energies, $V_{3z^2-r^2}$ = 2.43, $V_{x^2-y^2}$= 3.33, $V_{xz/yz}$= 1.41, V_{xy}= 1.93.

Parameters used in Ni^{4+} calculation (eV): Δ= -6.5, $10D_q$= 0.78, V_{eg}= 3.456, V_{t2g}= =2.004.

DFT Spectral Calculations

Density functional theory (DFT) calculations were carried out using the plane wave pseudopotential code CASTEP.[69] The Perdew-Burke-Ernzerhof (PBE) form of the generalized gradient approximation functional,[70] with the addition of the G06 semi-empirical dispersion correction[71] to better account for van der Waals forces. The $P2_1/c$ "zig-zag" Jahn-Teller distorted structure for $LiNiO_2$, and the $R\bar{3}m$ structure for NiO_2 were used to represent the pristine $LiNiO_2$ and fully delithiated materials respectively.[72] Each structure was initially geometry optimised using appropriate plane wave cut-off energies (900 eV) and k-points (0.03

$Å^{-1}$ k-point spacing) determined via convergence of the total energy. The geometry of the system was considered optimized when the maximum forces on the ions were below 0.001 eV/Å for NiO_2 and 0.01eV /Å for $LiNiO_2$ consistent with other studies.[72,73] Calculations of the pDOS and core-hole spectra were subsequently performed. The energy scale of the ground-state pDOS assumes the material is an insulator and sets the fermi energy, E_f, to zero. Since core orbitals are not treated explicitly in the pseudopotential method, a unique pseudopotential is generated for an excited atom possessing a core-hole. For O and Ni K-edges, a core-hole is placed on the O 1s or Ni 1s orbitals respectively. A supercell is generated to prevent interactions between neighbouring core-holes. For spectral calculations, the plane wave energy cut-off, k-point sampling and cell size were increased until no visible effect on the spectrum was seen. Spectral calculations were handled using the Optados programme.[74] Lorentzian broadening was performed using full widths at half maximum of 0.14 and 0.8 eV for the O and Ni K-edges respectively, which should reflect the lifetimes of radiative and non-radiative transitions.[75,76] The Gaussian component was then adjusted as a free parameter to best present the data but remained fixed for the same edges to allow for comparison. The Lorentzian component is given energy dependence to account for the energy dependence of the lifetime. This was done by summing the set width with a factor that varies linearly with energy as implemented in Optados. The calculated spectra were rigidly shifted to align with the first absorption peaks of the experimental data to allow better comparison. In cases where the system under investigation possessed more than one inequivalent excitation site, separate spectra were generated, energy aligned[77] and combined before rigidly shifting.

AUTHOR INFORMATION

Corresponding Author

*robert.weatherup@materials.ox.ac.uk

ACKNOWLEDGMENTS

The authors acknowledge funding from the Faraday Institution (faraday.ac.uk; EP/S003053/1, FIRG001, FIRG007, FIRG008, FIRG016, FIRG024) and the European Research Council (ERC) under the European Union's Horizon 2020 research and innovation programme (EXISTAR, grant agreement No. 950598) and under the Marie Sklodowska-Curie Actions (ISOBEL, grant agreement No. 101032281). We acknowledge support from the Engineering and Physical Science Research Council (EPSRC) through grants EP/K040375/1, EP/L022907/1, EP/T001038/1, and EP/R010145/1 (Henry Royce Institute). R.J.G. acknowledges funding from Natural Sciences and Engineering Research Council of Canada (NSERC). R.A.H. acknowledges funding from the Royal Academy of Engineering under the Research Fellowship scheme. R.S.W. acknowledges a CAMS-UK Fellowship through the Analytical Chemistry Trust Fund and a UKRI Future Leaders Fellowship (MR/V024558/1). We acknowledge access to the David Cockayne Centre for Electron Microscopy. We thank Diamond Light Source for beamtime on beamlines B07B, I10, and I20 under proposals SI33283, MM33062, and SP32010. We acknowledge the European Synchrotron Radiation Facility (ESRF) for provision of synchrotron radiation facilities under proposal MA-5753 and thank Blanka Detlefs for assistance and support in using beamline ID20.

REFERENCES

1. Wikner, E., Björklund, E., Fridner, J., Brandell, D. & Thiringer, T. How the utilised SOC window in commercial Li-ion pouch cells influence battery ageing. *Journal of Power Sources Advances* **8**, 100054 (2021).
2. Harlow, J. E. *et al.* A Wide Range of Testing Results on an Excellent Lithium-Ion Cell Chemistry to be used as Benchmarks for New Battery Technologies. *J Electrochem Soc* **166**, A3031–A3044 (2019).
3. International, A. *' This Is What We Die For': Human Rights Abuses in the Democratic Republic of the Congo Power the Global Trade in Cobalt*. (Amnesty International, 2016).
4. Wu, Z. *et al.* Unveiling the Evolution of LiCoO 2 beyond 4.6 V. *ACS Energy Lett* **8**, 4806–4817 (2023).
5. Lee, D. H., Gong, M., Lee, E. & Seo, D. H. Oxygen redox in LiNiO2 cathodes. *Joule* vol. 7 1408–1411 Preprint at https://doi.org/10.1016/j.joule.2023.06.023 (2023).
6. Kuiper, P., Kruizinga, G., Ghijsen, J., Sawatzky, G. A. & Verweij, H. Character of Holes in LixNi1−xO and Their Magnetic Behavior. *Phys Rev Lett* **62**, 1214–1214 (1989).
7. Mizokawa, T. *et al.* Role of oxygen holes in LixCoO2 revealed by soft X-ray spectroscopy. *Phys Rev Lett* **111**, 1–5 (2013).
8. Li, H., Zhang, N., Li, J. & Dahn, J. R. Updating the Structure and Electrochemistry of Li x NiO 2 for 0 ≤ x ≤ 1. *J Electrochem Soc* **165**, A2985–A2993 (2018).
9. Lee, S., Su, L., Mesnier, A., Cui, Z. & Manthiram, A. Cracking vs. surface reactivity in high-nickel cathodes for lithium-ion batteries. *Joule* vol. 7 2430–2444 Preprint at https://doi.org/10.1016/j.joule.2023.09.006 (2023).
10. Kong, F. *et al.* Kinetic Stability of Bulk LiNiO2 and Surface Degradation by Oxygen Evolution in LiNiO2-Based Cathode Materials. *Adv Energy Mater* **9**, 1802586 (2019).
11. Xu, J. *et al.* Elucidation of the surface characteristics and electrochemistry of high-performance LiNiO2. *Chemical Communications* **52**, 4239–4242 (2016).
12. Aurbach, D. *et al.* The Study of Surface Phenomena Related to Electrochemical Lithium Intercalation into LixMOy Host Materials (M = Ni, Mn). *J Electrochem Soc* **147**, 1322 (2000).
13. Ahmed, S. *et al.* Visualization of Light Elements using 4D STEM: The Layered-to-Rock Salt Phase Transition in LiNiO2 Cathode Material. *Adv Energy Mater* **10**, (2020).
14. Yoon, C. S., Jun, D. W., Myung, S. T. & Sun, Y. K. Structural Stability of LiNiO2 Cycled above 4.2 v. *ACS Energy Lett* **2**, 1150–1155 (2017).
15. de Biasi, L. *et al.* Phase Transformation Behavior and Stability of LiNiO 2 Cathode Material for Li-Ion Batteries Obtained from In Situ Gas Analysis and Operando X-Ray Diffraction. *ChemSusChem* **12**, 2240–2250 (2019).
16. Papp, J. K. *et al.* A comparison of high voltage outgassing of LiCoO2, LiNiO2, and Li2MnO3 layered Li-ion cathode materials. *Electrochim Acta* **368**, 137505 (2021).
17. Li, N. *et al.* Unraveling the Cationic and Anionic Redox Reactions in a Conventional Layered Oxide Cathode. *ACS Energy Lett* **4**, 2836–2842 (2019).
18. Juelsholt, M. *et al.* Does trapped O2 form in the bulk of LiNiO2 during charging ? *Energy Environ Sci* (2024) doi:10.1039/d3ee04354a.

19. Menon, A. S. *et al.* Oxygen-Redox Activity in Non-Lithium-Excess Tungsten-Doped Li Ni O 2 Cathode . *PRX Energy* **2**, 1 (2023).
20. Zhang, M. *et al.* Pushing the limit of 3d transition metal-based layered oxides that use both cation and anion redox for energy storage. *Nat Rev Mater* **7**, 522–540 (2022).
21. Li, N. *et al.* Unraveling the Cationic and Anionic Redox Reactions in a Conventional Layered Oxide Cathode. *ACS Energy Lett* **4**, 2836–2842 (2019).
22. Li, W., Reimers, J. N. & Dahn, J. R. In situ x-ray diffraction and electrochemical studies of Li1-xNiO2. *Solid State Ion* **67**, 123–130 (1993).
23. Bianchini, M., Roca-Ayats, M., Hartmann, P., Brezesinski, T. & Janek, J. There and Back Again—The Journey of LiNiO2 as a Cathode Active Material. *Angewandte Chemie - International Edition* **58**, 10434–10458 (2019).
24. Mock, M., Bianchini, M., Fauth, F., Albe, K. & Sicolo, S. Atomistic understanding of the LiNiO 2 –NiO 2 phase diagram from experimentally guided lattice models. *J Mater Chem A Mater* **9**, 14928–14940 (2021).
25. Chien, P. *et al.* New Insights into Structural Evolution of LiNiO 2 Revealed by Operando Neutron Diffraction. *Batter Supercaps* **4**, 1701–1707 (2021).
26. de Biasi, L. *et al.* Phase Transformation Behavior and Stability of LiNiO 2 Cathode Material for Li-Ion Batteries Obtained from In Situ Gas Analysis and Operando X-Ray Diffraction. *ChemSusChem* **12**, 2240–2250 (2019).
27. Li, W., Reimers, J. N. & Dahn, J. R. In situ x-ray diffraction and electrochemical studies of Li1-xNiO2. *Solid State Ion* **67**, 123–130 (1993).
28. Woolley, R. J., Illy, B. N., Ryan, M. P. & Skinner, S. J. In situ determination of the nickel oxidation state in La 2NiO4+δ and La4Ni3O 10-δ using X-ray absorption near-edge structure. *J Mater Chem* **21**, 18592–18596 (2011).
29. O'Grady, W. E., Pandya, K. I., Swider, K. E. & Corrigan, D. A. In Situ X-Ray Absorption Near-Edge Structure Evidence for Quadrivalent Nickel in Nickel Battery Electrodes. *J Electrochem Soc* **143**, 1613–1617 (1996).
30. Yano, J. & Yachandra, V. K. X-ray absorption spectroscopy. *Photosynthesis Research* vol. 102 241–254 Preprint at https://doi.org/10.1007/s11120-009-9473-8 (2009).
31. Menon, A. S. *et al.* Oxygen-Redox Activity in Non-Lithium-Excess Tungsten-Doped Li Ni O 2 Cathode. *PRX Energy* **2**, 13005 (2023).
32. Poletayev, A. D., Cottom, J. P., Morgan, B. J. & Islam, M. S. Temperature-Dependent Dynamic Disproportionation in LiNiO2. (2022).
33. Foyevtsova, K., Elfimov, I., Rottler, J. & Sawatzky, G. A. LiNiO2 as a high-entropy charge- and bond-disproportionated glass. *Phys Rev B* **100**, 1–7 (2019).
34. Mizokawa, T., Khomskii, D. & Sawatzky, G. Spin and charge ordering in self-doped Mott insulators. *Phys Rev B Condens Matter Mater Phys* **61**, 11263–11266 (2000).
35. Bisogni, V. *et al.* Ground-state oxygen holes and the metal-insulator transition in the negative charge-transfer rare-earth nickelates. *Nat Commun* **7**, 1–8 (2016).
36. Johnston, S., Mukherjee, A., Elfimov, I., Berciu, M. & Sawatzky, G. A. Charge disproportionation without charge transfer in the rare-earth-element nickelates as a possible mechanism for the metal-insulator transition. *Phys Rev Lett* **112**, 1–5 (2014).

37. Wawrzyńska, E. *et al.* Charge disproportionation and collinear magnetic order in the frustrated triangular antiferromagnet AgNiO2. *Phys Rev B Condens Matter Mater Phys* **77**, (2008).
38. Green, R. J., Haverkort, M. W. & Sawatzky, G. A. Bond disproportionation and dynamical charge fluctuations in the perovskite rare-earth nickelates. *Phys Rev B* **94**, 1–5 (2016).
39. Jin, L. *et al.* Hidden Hydroxides in KOH-Grown BaNiO3 Crystals: A Potential Link to Their Catalytic Behavior. *Chemistry of Materials* **35**, 9434–9443 (2023).
40. Huang, H. *et al.* Unusual double ligand holes as catalytic active sites in LiNiO2. *Nat Commun* **14**, 1–14 (2023).
41. Lebens-Higgins, Z. W. *et al.* Revisiting the charge compensation mechanisms in LiNi0.8Co0.2-: YAlyO2 systems. *Mater Horiz* **6**, 2112–2123 (2019).
42. Mikheenkova, A. *et al.* The role of oxygen in automotive grade lithium-ion battery cathodes: an atomistic survey of ageing. *J Mater Chem A Mater* **12**, 2465–2478 (2023).
43. Swallow, J. E. N. *et al.* Revealing solid electrolyte interphase formation through interface-sensitive Operando X-ray absorption spectroscopy. *Nat Commun* **13**, (2022).
44. Björklund, E. *et al.* Cycle-Induced Interfacial Degradation and Transition-Metal Cross-Over in LiNi0.8Mn0.1Co0.1O2-Graphite Cells. *Chemistry of Materials* **34**, 2034–2048 (2022).
45. Lin, F. *et al.* Surface reconstruction and chemical evolution of stoichiometric layered cathode materials for lithium-ion batteries. *Nat Commun* **5**, 3529 (2014).
46. Dose, W. M. *et al.* Electrolyte Reactivity at the Charged Ni-Rich Cathode Interface and Degradation in Li-Ion Batteries. *ACS Appl Mater Interfaces* **14**, 13206–13222 (2022).
47. Jung, R., Metzger, M., Maglia, F., Stinner, C. & Gasteiger, H. A. Oxygen Release and Its Effect on the Cycling Stability of LiNi x Mn y Co z O 2 (NMC) Cathode Materials for Li-Ion Batteries . *J Electrochem Soc* **164**, A1361–A1377 (2017).
48. Streich, D. *et al.* Operando Monitoring of Early Ni-mediated Surface Reconstruction in Layered Lithiated Ni-Co-Mn Oxides. *Journal of Physical Chemistry C* **121**, 13481–13486 (2017).
49. Yoon, W.-S. *et al.* Investigation of the Charge Compensation Mechanism on the Electrochemically Li-Ion Deintercalated Li 1-x Co 1/3 Ni 1/3 Mn 1/3 O 2 Electrode System by Combination of Soft and Hard X-ray Absorption Spectroscopy. *J Am Chem Soc* **127**, 17479–17487 (2005).
50. De Vries, A. H., Hozoi, L. & Broer, R. Origin of the chemical shift in X-ray absorption near-edge spectroscopy at the Mn K-edge in manganese oxide compounds. *Int J Quantum Chem* **91**, 57–61 (2002).
51. Miglio, A., Heinrich, C. P., Tremel, W., Hautier, G. & Zeier, W. G. Local Bonding Influence on the Band Edge and Band Gap Formation in Quaternary Chalcopyrites. *Advanced Science* **4**, 1700080 (2017).
52. De Groot, F. M. F. *et al.* 1s2p Resonant inelastic X-ray scattering of iron oxides. *Journal of Physical Chemistry B* **109**, 20751–20762 (2005).
53. Shadle, S. E., Hodgson, K. O., Solomon, E. I., Hedman, B. & Schugar, H. J. X-ray Absorption Spectroscopic Studies of the Blue Copper Site: Metal and Ligand K-Edge Studies To Probe the Origin of the EPR Hyperfine Splitting in Plastocyanin. *J Am Chem Soc* **115**, 767–776 (1993).

54. DeBeer, S. *et al.* X-ray absorption edge and EXAFS studies of the blue copper site in stellacyanin: Effects of axial amide coordination. *Journal of Physical Chemistry B* **104**, 10814–10819 (2000).
55. Chien, P. *et al.* New Insights into Structural Evolution of LiNiO 2 Revealed by Operando Neutron Diffraction. *Batter Supercaps* **4**, 1701–1707 (2021).
56. Delmas, C. *et al.* On the behavior of the LixNiO2 system: An electrochemical and structural overview. *J Power Sources* **68**, 120–125 (1997).
57. Li, W., Asl, H. Y., Xie, Q. & Manthiram, A. Collapse of LiNi1- x- yCoxMnyO2 Lattice at Deep Charge Irrespective of Nickel Content in Lithium-Ion Batteries. *J Am Chem Soc* **141**, 5097–5101 (2019).
58. Kondrakov, A. O. *et al.* Charge-transfer-induced lattice collapse in Ni-rich NCM cathode materials during delithiation. *Journal of Physical Chemistry C* **121**, 24381–24388 (2017).
59. Lee, S., Su, L., Mesnier, A., Cui, Z. & Manthiram, A. Cracking vs. surface reactivity in high-nickel cathodes for lithium-ion batteries. *Joule* **7**, 2430–2444 (2023).
60. Genreith-Schriever, A. R. *et al.* Oxygen hole formation controls stability in LiNiO2 cathodes. *Joule* **7**, 1623–1640 (2023).
61. Kong, F. *et al.* Kinetic Stability of Bulk LiNiO2 and Surface Degradation by Oxygen Evolution in LiNiO2-Based Cathode Materials. *Adv Energy Mater* **9**, 1–12 (2019).
62. de Biasi, L. *et al.* Phase Transformation Behavior and Stability of LiNiO2 Cathode Material for Li-Ion Batteries Obtained from In Situ Gas Analysis and Operando X-Ray Diffraction. *ChemSusChem* **12**, 2240–2250 (2019).
63. Koyama, Y., Mizoguchi, T., Ikeno, H. & Tanaka, I. Electronic structure of lithium nickel oxides by electron energy loss spectroscopy. *Journal of Physical Chemistry B* **109**, 10749–10755 (2005).
64. Van Der Laan, G., Zaanen, J., Sawatzky, G. A., Karnatak, R. & Esteva, J. M. Comparison of x-ray absorption with x-ray photoemission of nickel dihalides and NiO. *Phys Rev B* **33**, 4253–4263 (1986).
65. Huotari, S. *et al.* A large-solid-angle X-ray Raman scattering spectrometer at ID20 of the European Synchrotron Radiation Facility. *urn:issn:1600-5775* **24**, 521–530 (2017).
66. Sahle, C. J. *et al.* Planning, performing and analyzing X-ray Raman scattering experiments. *J Synchrotron Radiat* **22**, 400–409 (2015).
67. Haverkort, M. W. Quanty for core level spectroscopy - Excitons, resonances and band excitations in time and frequency domain. in *Journal of Physics: Conference Series* vol. 712 012001 (IOP Publishing, 2016).
68. Green, R. J., Haverkort, M. W. & Sawatzky, G. A. Bond disproportionation and dynamical charge fluctuations in the perovskite rare-earth nickelates. *Phys Rev B* **94**, 195127 (2016).
69. Clark, S. J. *et al.* First principles methods using CASTEP. *Zeitschrift fur Kristallographie* **220**, 567–570 (2005).
70. Perdew, J. P., Burke, K. & Ernzerhof, M. Generalized Gradient Approximation Made Simple. *Phys Rev Lett* **77**, 3865 (1996).
71. Grimme, S. Semiempirical GGA-type density functional constructed with a long-range dispersion correction. *J Comput Chem* **27**, 1787–1799 (2006).

72. Mock, M., Bianchini, M., Fauth, F., Albe, K. & Sicolo, S. Atomistic understanding of the LiNiO 2 –NiO 2 phase diagram from experimentally guided lattice models. *J Mater Chem A Mater* **9**, 14928–14940 (2021).
73. Chen, H., Freeman, C. L. & Harding, J. H. Charge disproportionation and Jahn-Teller distortion in LiNiO2 and NaNiO2: A density functional theory study. *Phys Rev B Condens Matter Mater Phys* **84**, 85108 (2011).
74. Morris, A. J., Nicholls, R. J., Pickard, C. J. & Yates, J. R. OptaDOS: A tool for obtaining density of states, core-level and optical spectra from electronic structure codes. *Comput Phys Commun* **185**, 1477–1485 (2014).
75. Perkins, S. T. *et al.* Tables and Graphs of Atomic Subshell and Relaxation Data Derived from the LLNL Evaluated Atomic Data Library, ${Z}=1-100$. *Eadl* **30**, UCRL-50400 (1991).
76. Campbell, J. L. & Papp, T. Widths of the atomic K-N7 levels. *At Data Nucl Data Tables* **77**, 1–56 (2001).
77. Eustace, D. A. *et al.* First-principles calculation of spectral features, chemical shift and absolute threshold of ELNES and XANES using a plane wave pseudopotential method. *J. Phys.: Condens. Matter* **21**, 6 (2009).